RSC Advances

PAPER

View Article Online
View Journal | View Issue

Cite this: *RSC Adv.*, 2020, **10**, 12298

Carbon electrode engineering for high efficiency all-inorganic perovskite solar cells†

Longfei Mi, *[ab] Yan Zhang,[b] Taotao Chen,[b] Enze Xu[b] and Yang Jiang *[b]

Received 10th January 2020
Accepted 11th March 2020

DOI: 10.1039/d0ra00288g

rsc.li/rsc-advances

Carbon-based inorganic perovskite solar cells (PSCs) have demonstrated an excellent performance in the field of photovoltaics owing to their simple fabrication techniques, low-cost and superior stability. Despite the lower efficiency of devices with a carbon electrode compared with the conventional structure, the potential applications in large scale have attracted increasing attention. Herein, we employ a mixed carbon electrode inorganic PSC by incorporating one-dimensional structure carbon nanotubes (CNTs) and two-dimensional Ti_3C_2-MXene nanosheets into a commercial carbon paste. This mixed carbon electrode, which is different from the pure carbon electrode in showing a point-to-point contact, provides a network structure and multi-dimensional charge transfer path, which effectively increases the conductivity of the carbon electrode and carriers transport. A respectable power conversion efficiency of 7.09% is obtained through carbon/CNT/MXene mixed electrode in $CsPbBr_3$-based solar cells.

1 Introduction

Hybrid organic–inorganic perovskite materials, as potential candidates in the solar energy conversion, have drawn considerable attention owing to their broad absorption wavelength (up to ~800 nm), strong absorption coefficient, high carrier mobility and facile processing techniques.[1–6] Since the first report in 2009 with an initial power conversion efficiency (PCE) of 3.8%,[7] a rapid development of hybrid organic–inorganic perovskite solar cells (PSCs) and various robust deposition techniques, *i.e.*, one-step/two-step solution strategy,[6,8–10] vapor deposition[11–15] and vapor-assisted solution method,[16–18] have ensured a champion PCE of above 25.2% in the past decade.[19] However, the perovskite solar cells (PSCs) based on the hybrid counterparts such as methylammonium lead halide ($MAPbX_3$) and formamidinium lead halide ($FAPbX_3$) suffers from the inferior stability because of the decomposition of fragile cation materials under moisture and thermal attacks, which impede their commercial applications in the future.[20,21]

The inorganic materials ($CsPbX_3$, X = I, Br and Cl) inherit the superior properties of hybrid counterparts and alleviate the instability issues of devices by substituting MA^+/FA^+ with inorganic cations such as cesium (Cs^+) and rubidium (Rb^+).[22–24] A record PCE of 18.3% and 10.9% for pure $CsPbI_3$ PSCs and $CsPbBr_3$ PSCs, respectively, have been achieved in recent studies, which makes the inorganic PSCs promising candidates in photovoltaics.[25–28] To date, the general configuration of PSCs employ the hole transfer layer (HTL), *i.e.*, spiro-OMeTAD, PTAA and NiO_x, which impedes them in the large scale in the realized application because of the high-cost of the organic transfer materials and extremely sensitive to humidity and thermal environment.[29–31] Very recently, a HTL-free structure is proposed by using a carbon paste as the counter electrode to replace the silver/gold electrode as well as HTL. For example, an all-inorganic $CsPbBr_3$-PSC with a carbon electrode was demonstrated, which showed an outstanding PCE of 9.7% accompanying with no performance degradation in moisture and heating conditions.[32] Similar to bromide-based PSCs, an α-$CsPbI_3$ HTL-free solar cell was constructed by employing a carbon electrode, and it presented a high efficiency of 9.5%.[33] Notably, this device showed a high stable performance and retained 90% of the initial efficiency. In addition, a mixed halide PSC, such as $CsPbI_2Br$ and $CsPbIBr_2$ inorganic PSCs, also exhibited high efficiency and high stability on combining with a carbon electrode,[34,35] which indicated that combining a carbon counter electrode to PSCs is a universal technique to improve the stability of all inorganic PSCs. The performances of the $CsPbBr_3$ PSCs with a carbon electrode are summarized in Table S1.† Although the initial PCE of the device without HTL is weaker than that containing HTL, it shows lower cost and better stability in air. Furthermore, the blade coating for depositing the carbon electrode, compared with the spin-coating, has been proposed as an innovative strategy in the commercial and academic fields because of the better continuous work and lower waste during the coating procedure.[36,37]

[a]*Department of Materials Science and Engineering, School of Civil Engineering, Qingdao University of Technology, Qingdao, Shandong, 266000, P. R. China. E-mail: mlf19881231@163.com*

[b]*School of Materials Science and Engineering, Hefei University of Technology, Hefei, Anhui, 230009, P. R. China*

† Electronic supplementary information (ESI) available. See DOI: 10.1039/d0ra00288g

It is worth noticing that the commercial carbon paste displays a point contact with the perovskite layer because of the particle-to-particle contact in the carbon electrode. Nevertheless, a large amount of pinholes exists at the interface of the carbon electrode/perovskite film, which is a serious concern for the carrier transport and shows a lower conductivity.[38] On the contrary, carbon nanotubes (CNTs) with a one-dimensional (1D) structure can provide high conductivity and direct transport path for carriers.[39] Simultaneously, Ti_3C_2-MXene displaying a two-dimensional (2D) layer structure gives an outstanding electrical conductivity and large surface area, which accelerate the carrier transport in the layer.[40–42]

In this study, we propose a novel mixed-carbon electrode by the incorporation of commercial carbon nanotubes and Ti_3C_2-MXene nanosheets into carbon paste, wherein the CNTs and MXene effectively increase the conductivity of the carbon electrode and carrier transport by constructing a three-dimensional (3D) carrier transfer path. A superior efficiency of 7.09% is achieved with a configuration of FTO/c-TiO_2/$CsPbBr_3$/mixed carbon. Furthermore, we anticipated that this mixed carbon electrode will pave a novel route for photovoltaics to enhance the efficiency and stability in the large-scale application in the future.

2 Materials and methods

2.1 $CsPbBr_3$ film

First, CsBr, $PbBr_2$ powder and clean substrates were placed into a vacuum chamber. Then, the chamber was pumped to a high vacuum degree of $\sim 10^{-3}$ Pa, and a heating source A was turned on to evaporate the CsBr with a speed of 0.5 Å s^{-1}. Further, the $PbBr_2$ powder was deposited at a rate of 0.8 Å s^{-1} in source B. Finally, the samples were annealed at a high temperature (300 °C) for 20 min in air to form an inorganic $CsPbBr_3$ thin film. The thickness of CsBr and $PbBr_2$ films in this experiment are 125 nm and 175 nm, respectively.

2.2 Mixed carbon paste

The commercial carbon paste and commercial carbon nanotubes were purchased from Shanghai MaterWin New Material. Co., Ltd and Shenzhen Sanshun Corporation, respectively. Ti_3AlC_2 powder was purchased from Jilin 11 Technology Co., Ltd. Following this the first step was to get Ti_3C_2-MXene. To etch the Ti_3AlC_2 powder, 20 ml of HF (40%) solution was used to dissolve 1 g of the raw powder and kept stirring for a whole day. After etching, deionized water was added for several times until the pH of the solution was above 5. Then, the as-prepared powders were moved to a vacuum drying oven to heat it for overnight (60 °C, 12 h). 0.5 g of $Ti_3C_2T_x$ powder was dissolved in 10 ml of a 25% tetramethylammonium hydroxide aqueous solution (TMAOH) to delaminate the $Ti_3C_2T_x$. After washing, centrifugation and sonication for several times, the Ti_3C_2-MXene nanosheets were obtained.[40] The mixed carbon paste was fabricated by mixing with the carbon paste for overnight. The weight ratio of carbon nanotubes and MXene are 1 : 0.5 : 0.1.

2.3 Device fabrication

Commercial FTO (7–8 Ω sq^{-1}) substrates were washed with acetone, ethyl alcohol and deionized water, respectively. Each step was done for 30 min. Then, the titanium isopropoxide precursor solution was spin-coated on FTO substrates at a speed of 2000 rpm for 40 s to form a compact TiO_2 layer. After sintering at 450 °C in air for 30 min, the substrates were treated with a $TiCl_4$ aqueous solution (40 mM) at 70 °C for 30 min and then annealed at 450 °C for another 30 min to get a high-quality c-TiO_2 thin film. The $CsPbBr_3$ inorganic perovskite absorption layer was deposited *via* a thermal evaporation method. A different kind of carbon ink was coated on the top layer of the perovskite film *via* doctor-blade coating as the counter electrode and was treated at 80 °C for several minutes in air.

2.4 Characterization

XRD measurements were conducted *via* XRD using Cu Kα X-ray radiation. Data were collected from 10° to 60° two theta degrees. The absorption and PL spectra were recorded using a UV-visible spectrophotometer (UV-2550) and a Hitachi F-4600 fluorescence spectrophotometer. SEM characterizations of the samples were performed using a scanning electron microscope (Sigma Zeiss and Hitachi SU8020). Current–voltage (*J–V*) plots of inorganic perovskite devices were measured using a Keithley 2636 system sourcemeter under an AM 1.5 G simulated solar illumination with a light intensity of ~100 mW cm^{-2}. The active area of each sample is 0.09 cm^2. All the tests were conducted in open air.

3 Result and discussion

The $CsPbBr_3$ perovskite film was fabricated *via* a two-step vapor deposition. As can be seen in Fig. 1a, the typical characteristic peaks of the as-prepared $CsPbBr_3$ film after annealing found at 15.18°, 21.55°, 26.48°, 30.64°, 34.37°, and 37.76° can be assigned to the (100), (110), (111), (200), (210) and (211) lattice planes. To analyze the optical properties of the sample, UV-vis absorption and photoluminescence (PL) were conducted, and the corresponding curves are displayed in Fig. 1b. A high PL peak at 528 nm and cut-off edge of light absorption spectrum at 550 nm can be seen clearly, which are consistent with those obtained in previous studies.[22,29] The top-view scanning electron microscope (SEM) images in Fig. 1c and d show a compact layer with a large grain size. The largest grain size of perovskite crystals is over 1 μm. This high crystallinity of perovskite grains can effectively reduce the defect density and is beneficial for the electron and hole separation and transport. Furthermore, the as-prepared film produced by the vapor deposition shows a smooth surface with a root-mean-square roughness (RMS) of 30.5 nm (Fig. 1e and f), which is beneficial for a better contact between the carbon electrode and perovskite layer.

The surface morphologies of pure carbon nanotubes, carbon paste and Ti_3C_2-MXene are shown in Fig. 2a–c, respectively. The long chain-like structure of CNTs accelerates them cross together to construct a continuous and crack-free thin film. Different from the one-dimensional structure, carbon powders show a spherical structure with a three-dimensional

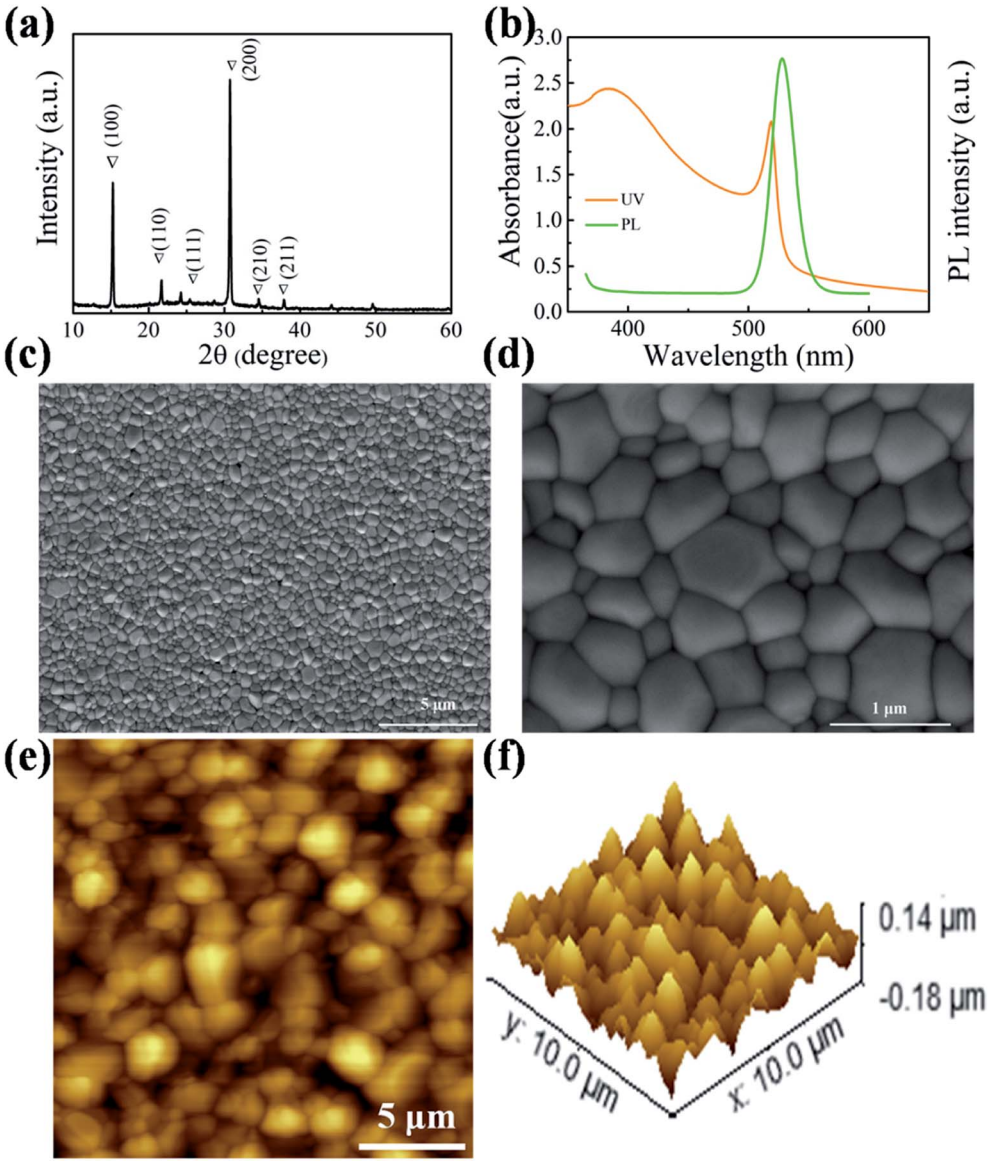

Fig. 1 (a) XRD pattern, (b) absorption and photoluminescence spectra of the $CsPbBr_3$ film; top view SEM images of the $CsPbBr_3$ thin film at (c) low and (d) high magnification. (e) 2D, (f) 3D atomic force microscopy characterizations of the $CsPbBr_3$ thin film.

architecture. Surprisingly, Ti_3C_2-MXene nanosheets present an accordion-like two-dimensional layer structure with a thickness of ~2 μm. After mixing and stirring, CNTs and Ti_3C_2-MXene can be well-distributed in the carbon paste (Fig. 2d and e). It is worth noticing that the particles closely pack because of the existence of a binder in the commercial carbon paste. The carbon powders are well coated with CNTs. Moreover, the voids of carbon powders are filled with MXene nanosheets (Fig. 2f). In this case, the carrier can be effectively collected and transported.

To further evaluate the performance of the mixed carbon electrode, a series of devices were assembled with a configuration of FTO/c-TiO_2/$CsPbBr_3$/mixed carbon (as shown in Fig. 3a), where TiO_2 and carbon serve as an electron transfer layer and counter electrode, respectively. The $CsPbBr_3$ thin film is an active layer, which can generate the electron and hole pairs under light illumination. The electron and hole will be separated and transported quickly to the FTO and counter electrode under built-in electric field.[43,44] Fig. 3b and c are the typical cross-section of devices with the mixed carbon electrode. The full coverage and continuous perovskite layer can be found in the SEM image. Good interface contact between the perovskite and carbon electrode ensures the hole transport to the counter electrode. Fig. 4a presents the current density–voltage (J–V) curves of the $CsPbBr_3$ solar cells with the mixed carbon electrode. The parameters voltage (V_{oc}), photocurrent density (J_{sc}) and fill factor (FF) are summarized in Table 1. The lower PCE of 4.77% for the devices with pure CNTs comes from the poor surface contact between the perovskite and counter electrode. Similarly, the device with pure carbon paste shows a higher PCE of 5.87% because of the better interface contact. However, the appearance of CNTs in the carbon electrode can significantly increase the photocurrent density due to the high mobility of CNTs. A respectable PCE of 7.09% with a V_{oc} of

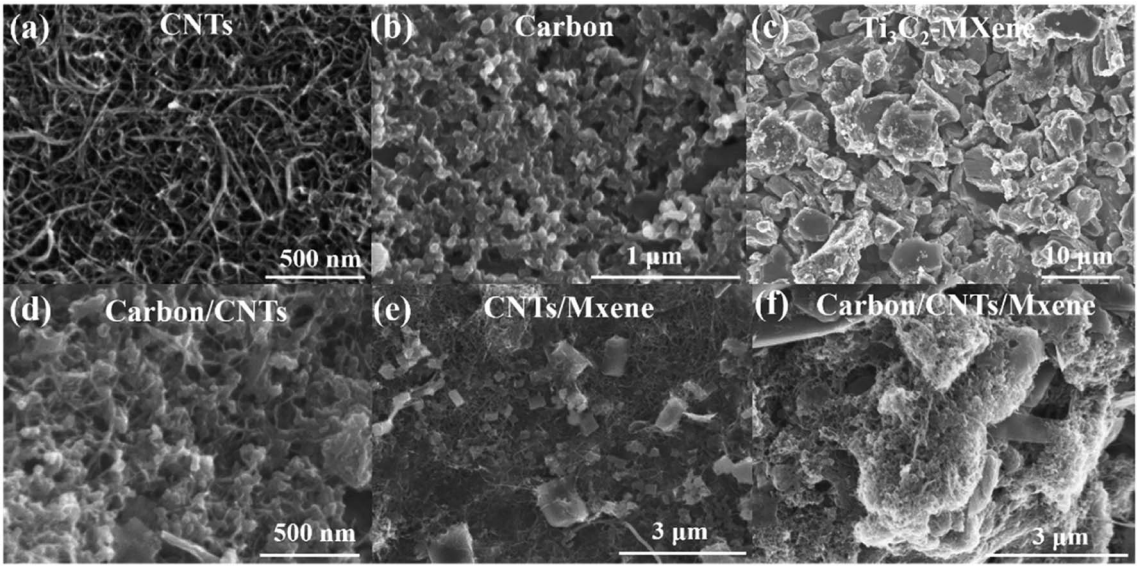

Fig. 2 Top-view SEM images of (a) CNTs, (b) carbon paste, (c) Ti_3C_2-MXene, (d) carbon/CNTs, (e) CNT/MXene and (f) carbon/CNT/MXene.

1.357 V, a J_{sc} of 7.16 mA cm^{-2} and an FF of 72.97% is obtained after the incorporation of CNTs and MXene into the carbon paste. As shown in Fig. S1 and Table S2,† the hysteresis of devices with mixed carbon electrodes was reduced in comparison with the pure carbon electrode $CsPbBr_3$ PSCs. The EQE spectrum in Fig. 4b displays a broad plateau of over 80% ranging from 350 to 500 nm. The corresponding photocurrent density extracted from the integration of EQE is closer to the value obtained from *J–V* curves. This excellent performance can be well explained by the carrier transport by mixed carbon. The pure carbon electrode shows a point-to-point contact, which means that the carrier transfer in the carbon electrode by particle-to-particle is expected to be much slow. With the appearance of CNTs, the one-dimensional structure provides a high-speed transport route for the carriers, which can accelerate the carrier transport. Moreover, MXene nanosheets are expected to improve the conductivity of the carbon electrode because of the higher conductivity and carrier mobility than graphene.[45] Most importantly, the small sizes of MXene can effectively fill in the voids in the carbon electrode and improve the contact of carbon particles. This point-line-layer contact structure is encouraged to improve the carbon electrode

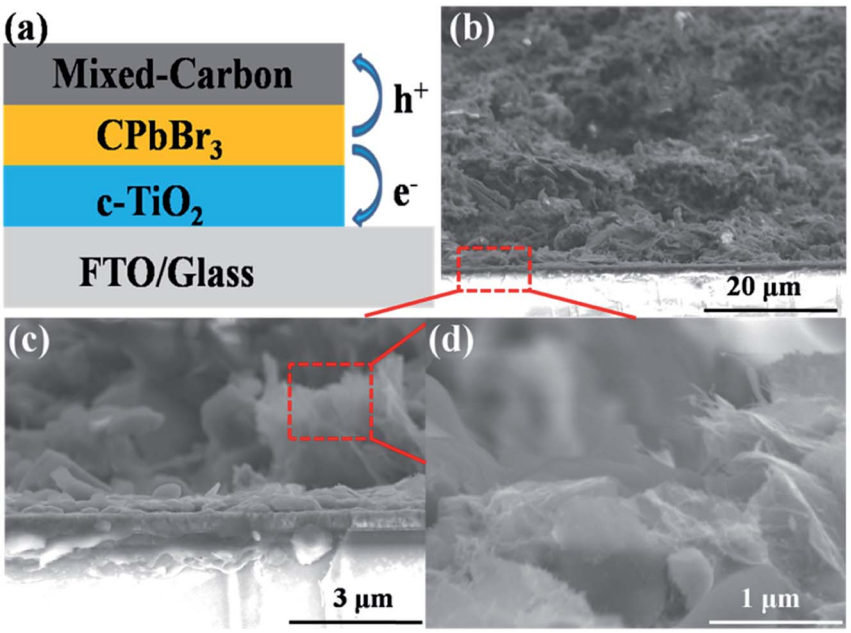

Fig. 3 (a) Schematic structure of the mixed carbon electrode $CsPbBr_3$ solar cell. Cross-section SEM images of (b) the device in a low magnification, (c) device in large magnification and (d) mixed carbon electrode.

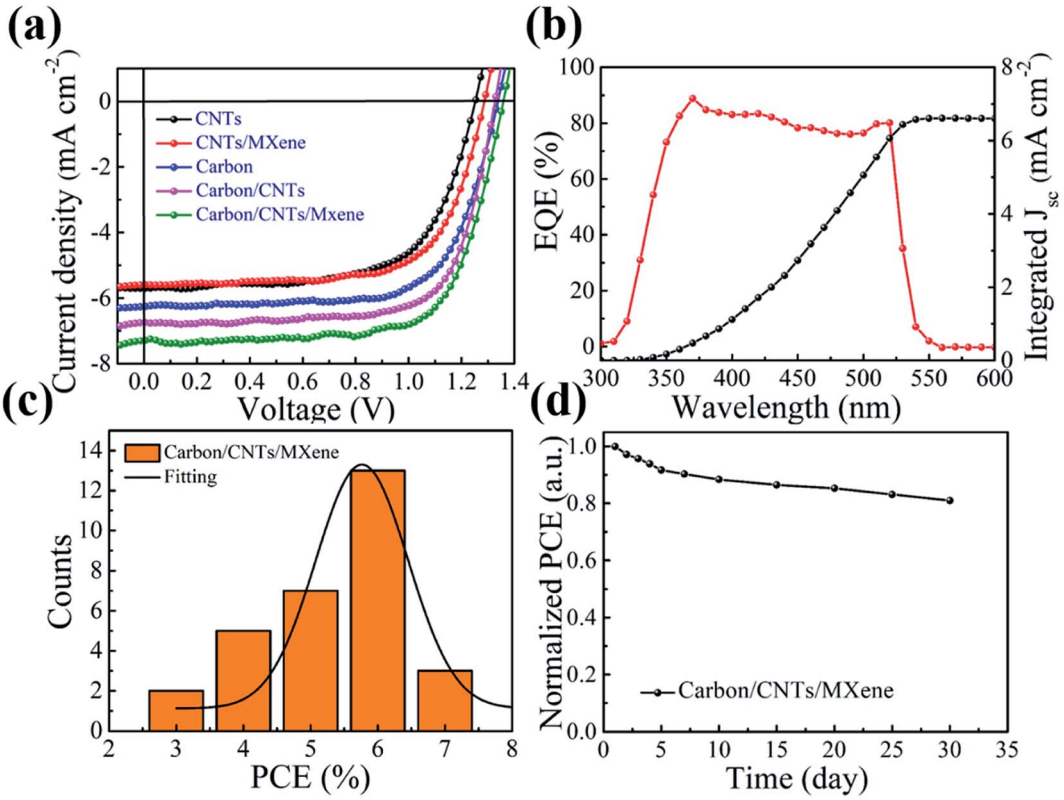

Fig. 4 (a) *J*–*V* curves of the devices with different types of electrodes. (b) EQE spectrum and corresponding integrated current density of the mixed carbon electrode $CsPbBr_3$ solar cell. (c) Statistical histogram of the PCEs of inorganic PSCs using mixed carbon electrodes. (d) Stability of devices in air with a humidity of RH = ~40%.

Table 1 Parameters of $CsPbBr_3$ PSCs with mixed carbon electrodes

Device	V_{oc} (V)	J_{sc} (mA cm^{-2})	FF (%)	PCE (%)
CNTs	1.250	5.81	65.68	4.77
CNT/MXene	1.286	5.52	69.73	4.95
Carbon	1.336	6.15	71.44	5.87
Carbon/CNTs	1.328	6.85	71.96	6.55
Carbon/CNT/MXene	1.357	7.16	72.97	7.09

conductivity and accelerates carrier transport. Furthermore, this mixed carbon electrode strategy displays a good repeatability. As seen in Fig. 4c, the PCEs of 30 devices are well distributed in a narrow range from 3% to 7%. The $CsPbBr_3$ solar cell using the mixed carbon electrode shows excellent stability in moisture. After storing in air for one month, the device kept 80% of the initial performance (Fig. 4d). The performance decrease is probably due to (1) the inevitable decomposition of $CsPbBr_3$ in moisture; (2) the oxidation of Ti_3C_2 to TiO_x caused by high humidity and oxygen in the air, which decrease the mobility of MXene and impede the carrier fast transport.[46]

4 Conclusion

In summary, we produced a high efficiency inorganic perovskite solar cell by introducing a mixed carbon electrode. The appearance of CNTs and Ti_3C_2-MXene can enhance the surface contact with carbon paste and promote the electrode conductivity. Moreover, compared with the traditional point-to-point transfer, the multi-dimensional charge transfer path can effectively improve the carrier extraction and transport, which produce an impressive PCE of 7.09%. These results show that the mixed carbon electrode can provide a novel method to prepare hole transport layer free inorganic PSCs with high PCE and has a potential for large scale applications in the future.

Conflicts of interest

There are no conflicts to declare.

Acknowledgements

We thanked the Qingdao University of Technology Staring Foundation (grant 20301721, 20302041), and National Natural Science Foundation of China (grant U1632151).

References

1 M. Liu, M. B. Johnston and H. J. Snaith, *Nature*, 2013, **501**, 395–398.
2 Y. Zhao and K. Zhu, *Chem. Soc. Rev.*, 2016, **45**, 655–689.

3 Z. Song, G. Tong, H. Li, G. Li, S. Ma, S. Yu, Q. Liu and Y. Jiang, *Nanotechnology*, 2018, **29**, 025401.
4 G. Tong, H. Li, Z. Zhu, Y. Zhang, L. Yu, J. Xu and Y. Jiang, *J. Phys. Chem. Lett.*, 2018, **9**, 1592–1599.
5 J. Shu, X. Zhang, P. Wang, R. Chen, H. Zhang, D. Li, P. Zhang and J. Xu, *Phys. B*, 2018, **548**, 53–57.
6 J. Lu, X. Sheng, G. Tong, Z. Yu, X. Sun, L. Yu, X. Xu, J. Wang, J. Xu, Y. Shi and K. Chen, *Adv. Mater.*, 2017, **29**, 1700400.
7 A. Kojima, K. Teshima, Y. Shirai and T. Miyasaka, *J. Am. Chem. Soc.*, 2009, **131**, 6050–6051.
8 N. J. Jeon, J. H. Noh, Y. C. Kim, W. S. Yang, S. Ryu and S. I. Seok, *Nat. Mater.*, 2014, **13**, 897–903.
9 D. Bi, C. Yi, J. Luo, J.-D. Décoppet, F. Zhang, S. M. Zakeeruddin, X. Li, A. Hagfeldt and M. Grätzel, *Nat. Energy*, 2016, **1**, 16142.
10 M. Xiao, F. Huang, W. Dkhissi, Y. Zhu, J. Etheridge, A. Gray-Weale, U. Bach, Y.-B. Cheng and L. Spiccia, *Angew. Chem., Int. Ed.*, 2014, **53**, 9898–9903.
11 G. Tong, H. Li, G. Li, T. Zhang, C. Li, L. Yu, J. Xu, Y. Jiang, Y. Shi and K. Chen, *Nano Energy*, 2018, **48**, 536–542.
12 L. K. Ono, M. R. Leyden, S. Wang and Y. B. Qi, *J. Mater. Chem. A*, 2016, **4**, 6693–6713.
13 C.-Y. Chen, H.-Y. Lin, K.-M. Chiang, W.-L. Tsai, Y.-C. Huang, C.-S. Tsao and H.-W. Lin, *Adv. Mater.*, 2017, **29**, 1605290–1605296.
14 Q. Ma, S. Huang, X. Wen, M. A. Green and A. W. Y. Ho-Baillie, *Adv. Energy Mater.*, 2016, **6**, 1502202.
15 G. Tong, Z. Song, G. Li, Y. Zhao, L. Yu, J. Xu, Y. Jiang, Y. Sheng and Y. Chen, *RSC Adv.*, 2017, **7**, 19457–19463.
16 D. Shan, G. Tong, Y. Cao, M. Tang, J. Xu, L. Yu and K. Chen, *Nanoscale Res. Lett.*, 2019, **14**, 208–213.
17 G. Tong, X. Lan, Z. Song, G. Li, H. Li, L. Yu, J. Xu, Y. Jiang, Y. Sheng and K. Chen, *Mater. Today Energy*, 2017, **5**, 173–180.
18 G. Tong, X. Geng, Y. Yu, L. Yu, J. Xu, Y. Jiang, Y. Sheng, Y. Shi and K. Chen, *RSC Adv.*, 2017, **7**, 18224–18230.
19 https://www.nrel.gov/pv/assets/pdfs/best-research-cell-efficiencies-190416.pdf, 2019.
20 J. Liang, J. Liu and Z. Jin, *Sol. RRL*, 2017, **1**, 1700086–1700109.
21 G. Tong, H. Li, D. Li, Z. Zhu, E. Xu, G. Li, L. Yu, J. Xu and Y. Jiang, *Small*, 2018, **14**, 1702523–1702530.
22 J. Liang, C. Wang, Y. Wang, Z. Xu, Z. Lu, Y. Ma, H. Zhu, Y. Hu, C. Xiao, X. Yi, G. Zhu, H. Lv, L. Ma, T. Chen, Z. Tie, Z. Jin and J. Liu, *J. Am. Chem. Soc.*, 2016, **138**, 15829–15832.
23 M. Saliba, T. Matsui, J.-Y. Seo, K. Domanski, J.-P. Correa-Baena, M. K. Nazeeruddin, S. M. Zakeeruddin, W. Tress, A. Abate, A. Hagfeldt and M. Grätzel, *Energy Environ. Sci.*, 2016, **9**, 1989–1997.
24 M. Saliba, T. Matsui, K. Domanski, J.-Y. Seo, A. Ummadisingu, S. M. Zakeeruddin, J.-P. Correa-Baena, W. R. Tress, A. Abate, A. Hagfeldt and M. Grätzel, *Science*, 2016, **354**, 206–209.
25 G. Tong and L. K. Ono, *Energy Technol.*, 2019, DOI: 10.1002/ente.201900961.
26 Y. Wang, T. Zhang, M. Kan and Y. Zhao, *J. Am. Chem. Soc.*, 2018, **140**, 12345–12348.
27 G. Tong, T. Chen, H. Li, L. Qiu, Z. Liu, Y. Dang, W. Song, L. K. Ono, Y. Jiang and Y. B. Qi, *Nano Energy*, 2019, **65**, 104015.
28 Y. Wang, M. I. Dar, L. K. Ono, T. Zhang, M. Kan, Y. Li, L. Zhang, X. Wang, Y. Yang, X. Gao, Y. B. Qi, M. Grätzel and Y. Zhao, *Science*, 2019, **365**, 591–595.
29 H. Li, G. Tong, T. Chen, H. Zhu, G. Li, Y. Chang, L. Wang and Y. Jiang, *J. Mater. Chem. A*, 2018, **6**, 14255–14261.
30 H. Yuan, Y. Zhao, J. Duan, Y. Wang, X. Yang and Q. Tang, *J. Mater. Chem. A*, 2018, **6**, 24324–24329.
31 K. Wang, Z. Jin, L. Liang, H. Bian, D. Bai, H. Wang, J. Zhang, Q. Wang and S. Liu, *Nat. Commun.*, 2018, **9**, 544.
32 J. Duan, Y. Zhao, B. He and Q. Tang, *Angew. Chem., Int. Ed.*, 2018, **57**, 3787–3791.
33 S. Xiang, Z. Fu, W. Li, J. Liu, H. Liu, L. Zhu, R. Zhang and H. Chen, *ACS Energy Lett.*, 2018, **3**, 1824–1831.
34 Z. Guo, S. Zhao, A. Liu, Y. Kamata, S. Teo, S. Yang, Z. Xu, S. Hayase and T. Ma, *ACS Appl. Mater. Interfaces*, 2019, **11**, 19994–20003.
35 Z. Guo, S. Teo, Z. Xu, C. Zhang, Y. Kamata, S. Hayase and T. Ma, *J. Mater. Chem. A*, 2014, **7**, 1227–1232.
36 A. Mei, X. Li, L. Liu, Z. Ku, T. Liu, Y. Rong, M. Xu, M. Hu, J. Chen, Y. Yang, M. Grätzel and H. Han, *Science*, 2014, **345**, 295–298.
37 G. Tong, T. Chen, H. Li, W. Song, Y. Chang, J. Liu, L. Yu, J. Xu, Y. B. Qi and Y. Jiang, *Sol. RRL*, 2019, **3**, 1900030.
38 Z. Wei, H. Chen, K. Yan, X. Zheng and S. Yang, *J. Mater. Chem. A*, 2015, **3**, 24226–24231.
39 S. N. Habisreutinger, R. J. Nicholas and H. J. Snaith, *Adv. Energy Mater.*, 2017, **7**, 1601839.
40 L. Yang, Y. Dall'Agnese, K. Hantanasirisakul, C. E. Shuck, K. Maleski, M. Alhabeb, G. Chen, Y. Gao, Y. Sanehira, A. K. Jena, L. Shen, C. Dall'Agnese, X.-F. Wang, Y. Gogotsi and T. Miyasaka, *J. Mater. Chem. A*, 2019, **7**, 5635–5642.
41 Z. Guo, L. Gao, Z. Xu, S. Teo, C. Zhang, Y. Kamata, S. Hayase and T. Ma, *Small*, 2018, **14**, 1802738.
42 T. Chen, G. Tong, E. Xu, H. Li, P. Li, Z. Zhu, J. Tang, Y. Qi and Y. Jiang, *J. Mater. Chem. A*, 2019, **7**, 20597–20603.
43 Q. Wang, Y. Shao, H. Xie, L. Lyu, X. Liu, Y. Gao and J. Huang, *Appl. Phys. Lett.*, 2014, **105**, 163508.
44 W. A. Laban and L. Etgar, *Energy Environ. Sci.*, 2013, **6**, 3249–3253.
45 H. Wang, Y. Wu, X. Yuan, G. Zeng, J. Zhou, X. Wang and J. W. Chew, *Adv. Mater.*, 2018, **30**, 1704561.
46 L. Yu, A. S. R. Bati, T. S. L. Grace, M. Batmunkh and J. G. Shapter, *Adv. Energy Mater.*, 2019, **11**, 1901063.